*Int. J. Engng Sci.* Vol. 29, No. 10, pp. 1315–1331, 1991
Printed in Great Britain. 

0020-7225/91 $3.00 + 0.00


# A STEADY STATE AXISYMMETRIC PENETRATION PROBLEM FOR RIGID/PERFECTLY PLASTIC MATERIALS

T. GOBINATH† and R. C. BATRA

Department of Mechanical and Aerospace Engineering and Engineering Mechanics, University of Missouri–Rolla, Rolla, MO 65401-0249, U.S.A.

**Abstract**—The axisymmetric deformations of an eroding long cylindrical rod made of a rigid/perfectly plastic material penetrating at a uniform rate into a thick rigid/perfectly plastic target are studied by the finite element method. It is assumed that the deformations appear steady to an observer situated at the stagnation point and moving with it, and that the contact between the target and the penetrator at the common interface is smooth. It is found that the resisting force experienced by the penetrator, the shape of the target/penetrator interface, and the distribution of normal tractions on it depend rather strongly upon the square of the penetration speed and also upon the ratio of the mass density of the penetrator to that of the target. In an attempt to help establish desirable testing regimes for practical problems we have also computed time histories of the hydrostatic pressure, second invariant of the strain-rate tensor and the spin for four typical penetrator and two typical target particles.

## INTRODUCTION

We study that phase of the penetration process in which the penetrator and target deformations appear steady to an observer located at the stagnation point and moving with it. This situation occurs when a very long cylindrical rod strikes a rather huge target and has penetrated a few rod diameters into it. Until the time either most of the rod has been eroded or the stagnation point reaches near the other end of the target, the penetration process can be regarded as being nearly steady and may constitute a significant part of the total penetration process. For moderately high striking speeds, Tate [1, 2] and Alekseevskii [3] modified the purely hydrodynamic approach by including the effects of the material strengths of the projectile and the target and representing them as some multiple of the yield strengths of the corresponding materials. However, the multiplying factor was unresolved in the theories. Pidsley [4] recently computed the values of the strength parameters for a copper rod penetrating into an aluminum target to be 2.4 $(\sigma_H)_t$ and $(-0.7)(\sigma_H)_p$ for the target and the penetrator, respectively. Here $\sigma_H$ equals the Hugoniot elastic limit of the material. He justified the negative value for the rod strength because of its yield stress being lower than that of the target.

The review paper of Backman and Goldsmith [5] provides a comprehensive summary of the work done on ballistic penetration until 1977, and discusses various physical mechanisms involved in the penetration and perforation processes and their engineering models. Also during the last decade engineering models of target penetration have been proposed by Ravid and Bodner [6], Ravid *et al.* [7], and Forrestal [8]. Some of the books on the subject are by Zukas *et al.* [9], Blazynski [10], Billington and Tate [11], and MaCauley [12].

In previous studies [13–19] Batra and his coworkers have analyzed the steady state penetration problem in which either the penetrator or the target was considered as rigid. Here we study the case when both deform and their materials can be modeled as rigid/perfectly plastic. As in [13–19], the contact between the penetrator and the target at the common interface is assumed to be smooth and no fracture or failure criterion is included. However, the effect of the penetration speed and the ratio of the mass densities of the penetrator and target on their deformations is investigated. We add that the problem studied herein is more challenging than those studied earlier in [13–19] because of the presence in it of two *a priori* unknown free surfaces, one the target/penetrator interface and the other the free surface of the penetrator material flowing backwards. Also the convective part of the acceleration plays a dominant role which requires the use of either an appropriately graded mesh or the use of

†Present address: EGS ADEPT, 25900 Greenfield, Oakpark, MI 48237, U.S.A.

artificial viscosity or both. The kinematic and stress fields found herein should help select improved kinematic fields in other approximate theories of penetration mechanics and also check results from simpler engineering theories of penetration.

An other outstanding problem in penetration mechanics is the selection of the appropriate constitutive models for the penetrator and target materials. In order to assess which one of the many recently proposed theories [20–23] of large deformation elastoplasticity is appropriate, and also help establish desirable testing regimes for practical problems, we compute histories of the second-invariant of the strain-rate tensor and the plastic spin for four penetrator and two target particles.

## FORMULATION OF THE PROBLEM

We use the Eulerian description of motion and a cylindrical coordinate system with origin at the stagnation point and moving with it at a uniform speed $v_s$ to describe the deformations of the penetrator and the target. The positive $z$-axis is taken to point towards the undeformed portion of the rod. Also we work in terms of non-dimensional variables indicated below by a superimposed bar.

$$\bar{\boldsymbol{\sigma}} = \boldsymbol{\sigma}/\rho v_s^2, \qquad \bar{p} = p/\rho v_s^2, \qquad \alpha = \rho v_s^2/\sigma_0,$$
$$\bar{\mathbf{v}} = \mathbf{v}/v_s, \qquad \bar{r} = r/r_0, \qquad \bar{z} = z/r_0. \tag{1}$$

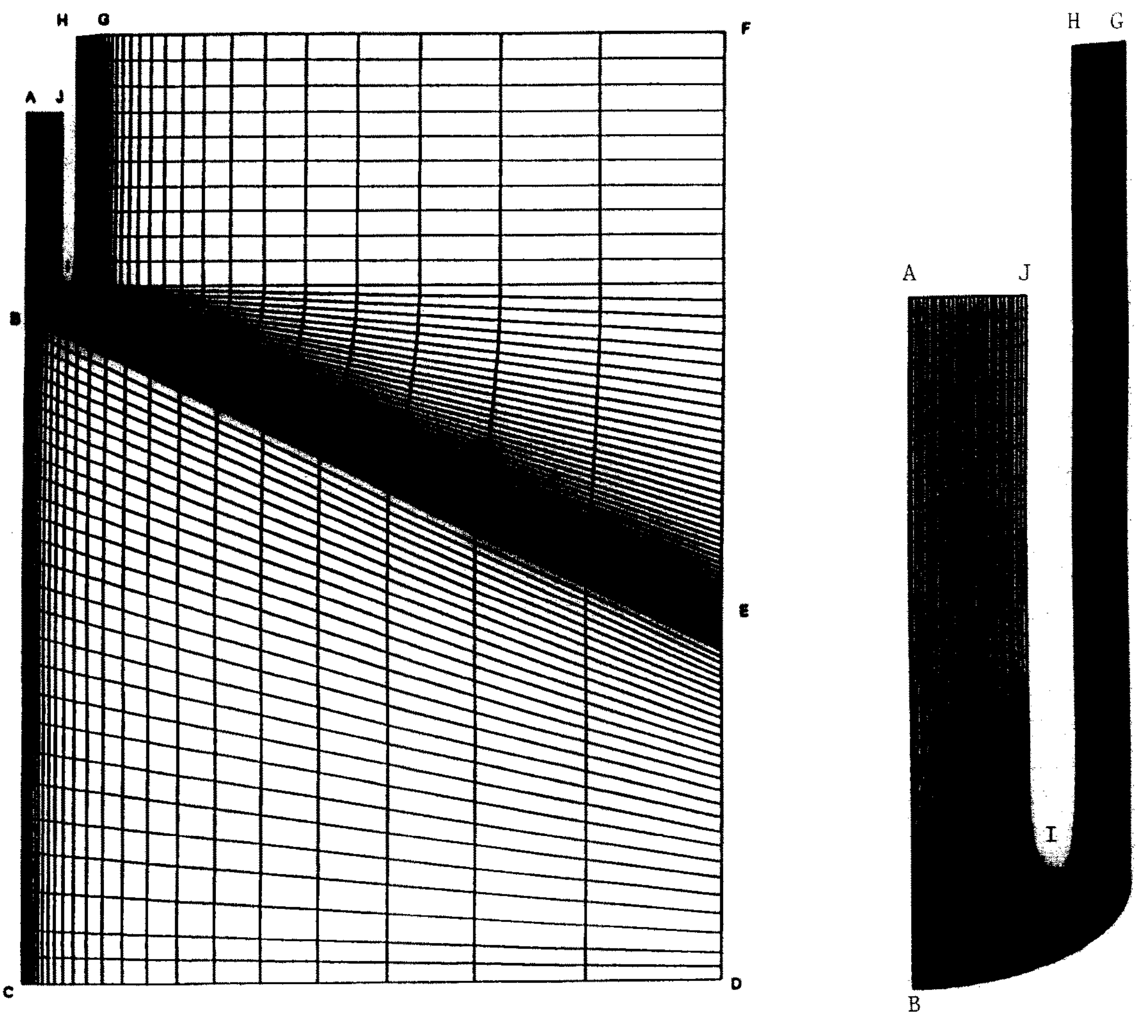


Fig. 1. The finite region studied and its discretization.

Here and below, $\boldsymbol{\sigma}$ is the Cauchy stress tensor, $p$ the hydrostatic pressure not determined by the deformation history because the deformations are assumed to be isochoric, $\mathbf{v} = (v_r, v_z)$ is the velocity of a material particle, and $r_0$ is the radius of the undeformed cylindrical portion of the penetrator. The non-dimensional parameter $\alpha$ equals the magnitude of the inertia forces relative to the flow stress of the material. When non-dimensionalizing a quantity for the penetrator and the target, the value of the corresponding material parameter is used in equation (1). An advantage of the non-dimensionalization (1) is that the equations governing the deformations of the penetrator and target look alike. Hereafter we use only non-dimensional variables and drop the superimposed bars. The governing equations can be written as

$$\operatorname{div} \mathbf{v} = 0, \tag{2.1}$$

$$\operatorname{div} \boldsymbol{\sigma} = (\mathbf{v} \cdot \operatorname{grad})\mathbf{v}, \tag{2.2}$$

$$\boldsymbol{\sigma} = -p\mathbf{1} + \frac{1}{\alpha\sqrt{3}\, I}\mathbf{D}, \tag{2.3}$$

$$2\mathbf{D} = \operatorname{grad} \mathbf{v} + (\operatorname{grad} \mathbf{v})^T, \tag{2.4}$$

$$2I^2 = \operatorname{tr}(\mathbf{D}^2). \tag{2.5}$$

Equation (2.1) expresses the balance of mass, (2.2) the balance of linear momentum, and equation (2.3) is the constitutive relation for the penetrator and target materials. Recall that the value of $\alpha$ will be different for them. $\mathbf{D}$, given by equation (2.4), is the strain-rate tensor and its second invariant is denoted by $I$. Equations (2.1) and the one obtained by substituting (2.3) into (2.2) are the field equations to be solved for $p$ and $\mathbf{v}$ under the appropriate boundary conditions.

A numerical solution of the problem usually necessitates that we consider only a finite region which for the Eulerian description of motion is also referred to as the control volume. The finite regions for the penetrator and target studied are depicted in Fig. 1, which also shows its finite element discretization. In the dark regions, a very fine finite element mesh is used. For the boundary conditions, we take

$$\mathbf{t} \cdot (\boldsymbol{\sigma}\mathbf{n}) = 0 \quad \text{on } \Gamma_i, \tag{3.1}$$

$$\mathbf{n} \cdot \boldsymbol{\sigma}_t \mathbf{n} = (\rho_p/\rho_t)\mathbf{n} \cdot \boldsymbol{\sigma}_p \mathbf{n} \quad \text{on } \Gamma_i, \tag{3.2}$$

$$\mathbf{v} \cdot \mathbf{n} = 0 \quad \text{on } \Gamma_i, \tag{3.3}$$

$$\boldsymbol{\sigma}\mathbf{n} = \mathbf{0} \quad \text{on } \Gamma_f, \tag{3.4}$$

$$\mathbf{v} \cdot \mathbf{n} = 0 \quad \text{on } \Gamma_f, \tag{3.5}$$

$$\sigma_{rz} = 0, \quad v_r = 0 \quad \text{on the axis of symmetry } ABC, \tag{3.6}$$

$$v_z = 1, \quad v_r = 0 \quad \text{on the boundary surfaces } CD \text{ and } DEF, \tag{3.7}$$

$$\sigma_{zz} = 0, \quad v_r = 0 \quad \text{on } FG, \tag{3.8}$$

$$v_z = v_e, \quad \sigma_{rz} = 0 \quad \text{on the outlet surface } GH, \tag{3.9}$$

$$v_z = -(v_p - 1), \quad v_r = 0 \quad \text{on the inlet surface } AJ. \tag{3.10}$$

Here $\Gamma_i$ is the target/penetrator interface $BG$, and $\Gamma_f$ is the free surface $JIH$ of the deformed penetrator. The condition (3.1) expresses the assumption that the contact between the penetrator and target is frictionless, therefore, the tangential tractions there vanish. This seems reasonable since a thin layer of the material at the interface either melts or is severely degraded by adiabatic shear. The boundary condition (3.2) states that the normal tractions across the common interface $\Gamma_i$ are continuous, and equation (3.3) implies that $\Gamma_i$ is a streamline. If $\Gamma_i$ were known, then either (3.2) or (3.3) is required. Here we use (3.2) to verify that the assumed shape of $\Gamma_i$ is reasonably correct as discussed in the next section. The boundary condition (3.4) asserts that $\Gamma_f$ is a free surface, and equation (3.5) implies that it is a streamline. Equation (3.5) is used to ensure that the assumed shape of $\Gamma_f$ is close to the actual one. The boundary condition (3.6) follows from the assumption that the deformations are axisymmetric. Since the distances of $CD$ and $DF$ from $\Gamma_i$ exceed 30 $r_0$, and significant target deformations occur in the target region distance at most $2r_0$ from $\Gamma_i$, it is reasonable to assume that target particles on the bounding surfaces $CD$ and $DF$ do not deform. If the surfaces $FG$ and $GH$ were situated at infinite distances from the stagnation point $B$, then the boundary conditions (3.8) and (3.9) on them will hold exactly. Since these surfaces are situated at a distance of nearly $7r_0$ from $B$, the boundary conditions (3.8) and (3.9) are good approximations. The value of $v_e$ in equation (3.9) is estimated by using the balance of mass for the penetrator region. The boundary condition (3.10) states that the end $AJ$ of the rod has not deformed and is moving downward with a uniform speed. For an assigned value of $v_s$, $v_p$ is estimated from the relation [1]

$$\frac{1}{2}(v_p-1)^2+Y_p=\left(R_t+\frac{1}{2}\right)\left(\frac{\rho_t}{\rho_p}\right) \tag{4}$$

where $Y_p$ and $R_t$ represent strength parameters for the penetrator and target materials. In his 1967 paper Tate [1] found $R_t = 3.5(\sigma_H)_t$ and in a recent paper [24] he gave $Y_p = 1.7\sigma_{0p}$, $R_t = \sigma_{0t}(2/3 + \ln(0.57E_t/\sigma_{0t}))$, where $E_t$ is Young's modulus for the target material. Batra and Chen [25] used a semianalytical method to analyze the steady state axisymmetric deformations of a viscoplastic target being penetrated by a rigid hemispherical nosed penetrator and found that

$$R_t = 9.43\sigma_{0t}.$$

In terms of dimensional variables, we need to know $(R_t - Y_p)$ rather than the values of $R_t$ and $Y_p$ to find $v_p$ from equation (4).

## COMPUTATIONAL CONSIDERATIONS

The aforestated problem was solved by the following iterative technique. Assume $\Gamma_i$ and $\Gamma_f$. Then the regions $R_p$ (shown in Fig. 1 by the closed curve ABGHIJA) and $R_t$ (shwn in Fig. 1 by the closed curve BCDEFGB) occupied, respectively, by the deformating penetrator and target material are well defined. The governing equations (2) under the boundary conditions (3.1), (3.3), (3.4), (3.6), (3.9), and (3.10) are solved to find the fields of $(\mathbf{v}, p)$ for the penetrator, and equations (2) under the boundary conditions (3.1), (3.3), (3.6), (3.7), and (3.8) are solved to find the fields of $(\mathbf{v}, p)$ for the target. The boundary conditions (3.2) and (3.5) are used to verify that the assumed $\Gamma_i$ and $\Gamma_f$ are reasonably correct. We first adjust $\Gamma_f$, and then $\Gamma_i$ always ensuring that $\Gamma_f$ is still correct and, if necessary, $\Gamma_f$ is readjusted. During the modification of $\Gamma_i$, nodes on it are moved in a direction perpendicular to $\Gamma_i$ by an amount proportional to $(f_p^n - f_t^n)$. Here $f_p^n$ and $f_t^n$ equal, respectively, the normal force on a penetrator and target particle on $\Gamma_i$.

The algorithm developed by Batra and Lin [16] to adjust $\Gamma_f$ was modified to increase its efficiency and has been described by Gobinath and Batra [26]. After new shapes of $\Gamma_i$ and $\Gamma_f$ have been determined, a check is made to ensure that the elements adjoining these surfaces have not been severely distorted. If necessary, a new mesh is generated by solving on $R_p$ and $R_t$ the Laplace equation $\nabla^2\phi = 0$ under the essential boundary conditions $\phi = r$ and $\phi = z$. The intersection of the equipotential curves gives the new location of the nodes.

We used 9-noded quadrilateral macroelements each of which was divided into four 4-noded quadrilateral elements called microelements. In each micro-element the velocity field was assumed to be bilinear and pressure constant. The variables corresponding to the central node were eliminated prior to the assembly of the global stiffness matrix. An artificial viscosity $\nu$ given by [27]

$$\nu = \nu_r + \nu_z, \tag{5.1}$$

$$\nu_r = h_r(\coth \nu_1 - 1/\nu_1)/2, \tag{5.2}$$

$$\nu_z = h_z(\coth \nu_2 - 1/\nu_2)/2, \tag{5.3}$$

$$\nu_1 = \sqrt{3}\, v_r^c h_r I^c/\alpha, \qquad \nu_2 = \sqrt{3}\, v_z^c h_z I^c/\alpha, \tag{5.4}$$

was added to $\alpha/\sqrt{3}I$ in equation (2.3). In these equations $h_r$ and $h_z$ equal, respectively, the largest distances in the $r$ and $z$ directions between the midpoints of the sides of a quadrilateral, and the superscript $c$ denotes that the quantity is evaluated at the centroid of an element. Brooks and Hughes [27] have shown that adding artificial viscosity is equivalent to using the Petrov–Galerkin approximation of equations (2.2)–(2.5).

## DISCUSSION OF RESULTS

Recalling that the governing equations for the velocity field are nonlinear, the solution was assumed to have converged when, at each nodal point, the value of the speed computed during two successive iterations differed by no more than 5%. The convergence criterion used for the free surface $\Gamma_f$ was that at each node point on $\Gamma_f$, $|\mathbf{v}\cdot n|\leq 0.02$, and that for $\Gamma_i$

$$|f_p^n - f_t^n| \leq 0.025[|f_p^n| + |f_t^n|], \tag{6}$$

at each node point on it. These convergence criteria are stronger than the global norms of errors sometimes employed.

### *Results for different speeds of penetration*

We set

$$\rho_p = \rho_t = 7800\,\text{kg/m}^3, \qquad \sigma_{0p} = 350\,\text{MPa}, \qquad \sigma_{0t} = 114.3\,\text{MPa}, \tag{7}$$

and compute results for $v_s = 400$ m/s, 500 m/s and 600 m/s. The corresponding values of $(\alpha_p, \alpha_t)$ are (3.57, 10.92), (5.57, 17.06), and (8.02, 24.57), respectively. Values of $v_p$, as computed from equation (4), with $R_t - Y_p = 164.35$ MPa, equal 850 m/s, 1041 m/s and 1234 m/s for the three values of $v_s$ considered herein. Since $\alpha_t \simeq 3\alpha_p$, the inertia forces play a more dominant role for the target deformations as compared to that for the deformations of the penetrator. Figure 2 depicts the shapes of the free surface $\Gamma_f$ and the target/penetrator interface $\Gamma_i$ for these three values of $v_s$. In these plots the ordinate is the vertical distance from the bottom-most surface $CD$ of the target region studied in order to decipher the vertical movement of $\Gamma_i$ and $\Gamma_f$. When plotting $\Gamma_f$, the horizontal scale has been enlarged enormously to magnify the small differences in the shapes of the free surface for the three values of $v_s$. The

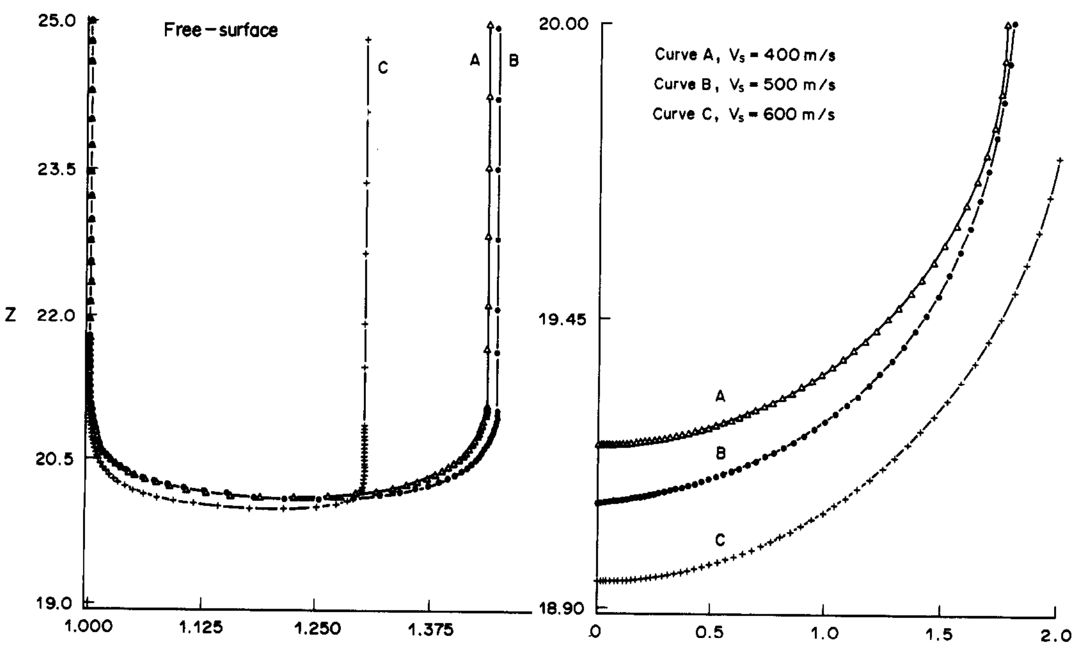


Fig. 2. Shapes of the free surface of the deformed penetrator and the target/penetrator interface for three different speeds.

shapes of $\Gamma_i$ in the vicinity of the stagnation point seem to be independent of $v_s$. A least squares fit to the curve for $v_s = 600$ m/s has the equation

$$\frac{r^2}{2.061^2} + \frac{(z-1.05)^2}{1.05^2} = 1. \tag{8}$$

It is interesting to note that Tate [28] found the equation of the bottom surface of $\Gamma_i$ to be

$$\frac{r^2}{(1.155a)^2} + \frac{(z-a)^2}{a^2} = 1.$$

A possible reason for the difference in the value of the coefficient for the first term is the lower value of $v_s$ considered here.

The mean normal tractions at the common interface $\Gamma_i$ for the three values of $v_s$ are plotted in Fig. 3. Also shown in the figure is a least squares fit to the data points ($F_a$, $\alpha_t$) where $F_a$ is the non-dimensional axial resisting force experienced by the penetrator; the corresponding dimensional force equals $(\pi r_0^2 \sigma_{0p})F_a$. It was found that the quadratic curve

$$F_a = 5.323 + 1.101\alpha_t + 0.031\alpha_t^2, \quad 10.92 \leq \alpha_t \leq 24.57, \tag{9}$$

provided a better fit to the computed data than a straight line. Batra and Lin [16] who studied the deformations of a rigid/perfectly plastic cylindrical rod upset at the bottom of a rigid cavity $z = 0.04r^4$ found $F_a = -2.2 + 2.15\alpha_p$, $1.8 \leq \alpha_p \leq 6$. In each of these cases, the values of $F_a$ depend rather noticeably upon $\alpha_t$ and/or $\alpha_p$. The normal tractions on $\Gamma_i$ increase significantly with an increase in $v_s$. The general shapes of these curves especially near the stagnation point do not vary, and they are shifted upwards with an increase in $v_s$. For values of the non-dimensional arc length exceeding 2, the normal tractions on $\Gamma_i$ become exceedingly small. At the stagnation point, the normal traction on $\Gamma_i$ equals $(-\sigma_{zz})$, and since uniaxial strain conditions prevail on the axial line, $s_{zz} = (\sigma_{zz} + p)$ equals $(2/3\sigma_0)$ there. For penetrator and target particles on the axial line and situated within $2r_0$ of the stagnation point, computed values of $|s_{zz} - 2\sigma_0/3|$ were less than 0.02. Since $\sigma_{zz} \gg \sigma_0$ at the stagnation point, the hydrostatic pressure $p_0$ there provides a predominant contribution to $\sigma_{zz}$. The least squares fit

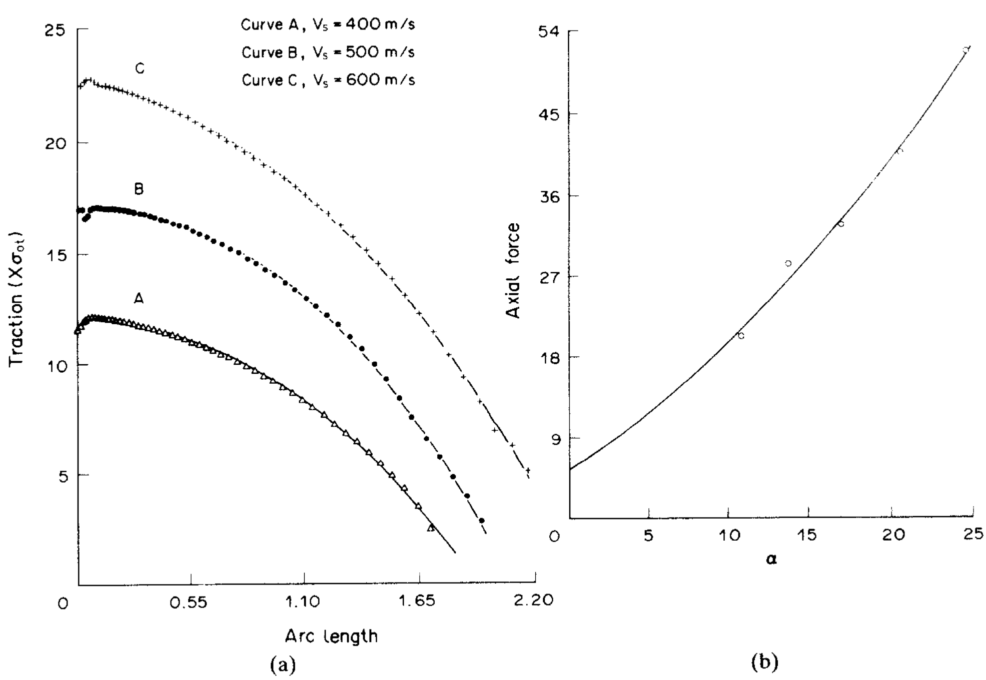


Fig. 3. (a) Distribution of the mean normal tractions on the target/penetrator interface for three different speeds. (b) Dependence of the axial resisting force experienced by the penetrator upon the non-dimensional number $\alpha_t$.

to the data points $(p_{0p}, \alpha_p)$, $(p_{0t}, \sigma_t)$, have the equations

$$p_{0p} = (0.1084 + 0.884\alpha_p)\sigma_{0p}, \tag{10.1}$$

$$p_{0t} = (4.005 + 0.683\alpha_t)\sigma_{0t}, \tag{10.2}$$

for the penetrator and the target respectively.

Recalling that equations,

$$\frac{1}{2}\rho_p(v_p - v_s)^2 + Y_p = \frac{1}{2}\rho_t v_s^2 + R_t = -(\sigma_{zz})_s, \tag{11}$$

proposed by Alekseevskii [3] and Tate [1], where $Y_p$ and $R_t$ equal the resistive pressure terms due to the strength of the material, $(\sigma_{zz})_s$ is the value of $\sigma_{zz}$ at the stagnation point $B$, and quantities are dimensional, hold on the axial line we can find the values of $R_t$ and $Y_p$. The computed values of $R_t$ and $Y_p$ for the three penetration speeds studied are listed in Table 1.

Table 1

| $v_s$ (m/s) | $R_t$ $(x\sigma_{0t})$ | $Y_p$ $(x\sigma_{0p})$ |
|---|---|---|
| 400 | 6.19 | 1.553 |
| 500 | 8.46 | 2.293 |
| 600 | 10.29 | 2.89 |

We should caution the reader that equations (10.1) and (10.2) were obtained by a least squares fit to the data. Substitution from (10.1) and (10.2) into (11) and setting $(s_{zz})_s = 2/3\sigma_{0p}$ or $2/3\sigma_{0t}$ may yield values of $Y_p$ and $R_t$ that are slightly different from those listed in the table.

*Results for different ratios of mass densities*

In Fig. 4(a) are plotted the shapes of the free surface of the deformed penetrator and of the target/penetrator interface for $\rho_t/\rho_p = 1.25$, 1.0 and 0.75. The ordinate is the vertical distance from the bottom surface $CD$ of the target region considered. In these computations $\rho_p$ was kept fixed and $v_s$ was set equal to 500 m/s. For $\rho_t/\rho_p = 0.75$, the bottom portion of the free surface is slightly above that for $\rho_t/\rho_p = 1.0$, and for $\rho_t/\rho_p = 1.25$, the bottom part of the free surface moves a little below that for $\rho_t/\rho_p = 1.0$. The curvature of the free surface where the flow turns upwards also seems to depend on $\rho_t/\rho_p$. The stagnation point does not move much when $\rho_t/\rho_p$ is changed from 1.00 to 0.75 implying thereby that the thickness of the deforming penetrator material between the target/penetrator interface and the free surface of the deformed penetrator, especially near the axial line, is larger for $\rho_t/\rho_p = 0.75$ as compared to that for $\rho_t/\rho_p = 1.0$. When $\rho_t/\rho_p$ is changed from 1.0 to 1.25, both the stagnation point and the bottom part of the free surface $\Gamma_f$ move lower and since the former moves by a larger distance, the thickness of the deforming penetrator material between $\Gamma_i$ and $\Gamma_f$ increases again. The normal tractions on $\Gamma_i$, plotted in Fig. 4(b), reveal that the largest normal tractions occur for $\rho_t/\rho_p = 1.25$ and least for $\rho_t/\rho_p = 0.75$ and the change seems to depend continuously upon $\rho_t/\rho_p$. Thus, for the same penetrator material, the pressure at the stagnation point will increase with an increase in the mass density of the target; and for a given target, higher density penetrators would result in smaller values of the pressure at the stagnation point.

Values of $R_t$ and $Y_p$, computed by using equation (11) and $v_s = 600$ m/s, for different values of $\rho_t/\rho_p$ are listed in Table 2.

We note that Pidsley [4] found for $\rho_t/\rho_p = 0.313$, $R_t = 2.4(\sigma_H)t$ and $Y_p = -0.7(\sigma_H)p$. For many materials the Hugoniot elastic limit equals approximately 1.6 times the yield strength in a quasistatic simple compression test [1].

*Results for a fixed value of $v_s$*

The contours of the non-dimensional hydrostatic pressure for $v_s = 600$ m/s are shown in Fig. 5. These values ought to be multipled by 8.02 and 24.57 for the penetrator and target to obtain

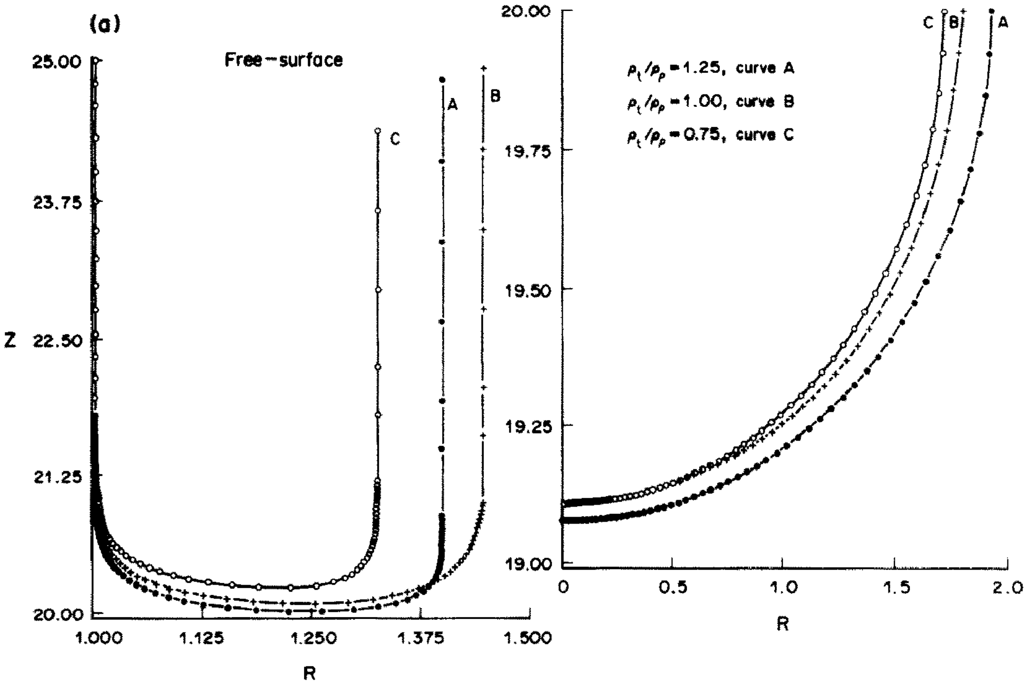


Fig. 4(a). Shapes of the free surfaces of the deformed penetrator and the target/penetrator interface for three different values of $\rho_t/\rho_p$.

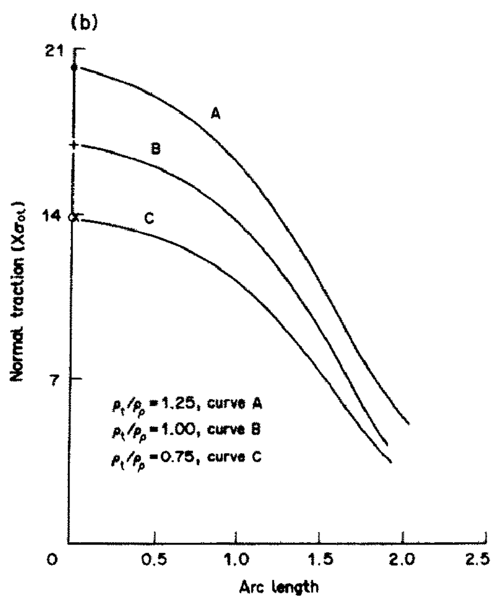


Fig. 4(b). Distribution of mean normal tractions on the target/penetrator interface for three different values of $\rho_t/\rho_p$. Curve A, $\rho_t/\rho_p = 1.25$; Curve B, $\rho_t/\rho_p = 1.0$; Curve C, $\rho_t/\rho_p = 0.75$.

Table 2

| $(\rho_t/\rho_p)$ | $R_t$ $(x\sigma_{0t})$ | $Y_p$ $(x\sigma_{0p})$ |
|---|---|---|
| 0.75 | 7.448 | 1.963 |
| 1.0 | 8.46 | 2.293 |
| 1.25 | 9.49 | 2.63 |

values of $p$ as a multiple of corresponding $\sigma_0$. Thus $p_{max}$ equals $7.3\sigma_{0p}$ in the penetrator and $20.8\sigma_{0t}$ in the target for $\alpha_p = 8.02$ and $\alpha_t = 24.57$. We note that for the hemispherical nosed rigid penetrator and a rigid/perfectly plastic target Batra and Wright [13] computed $p_{max}$ to be $8.0\sigma_{0t}$ for $\alpha_t = 6.15$ and Batra and Lin [19] found $p_{max} = 3\sigma_{0p}$ for $\alpha_p = 5.1$ for a rigid/perfectly plastic cylindrical rod striking a rigid cavity. The variation of the hydrostatic pressure on the axial line, also depicted in Fig. 5, reveals that the pressure decays quickly in the penetrator and rather slowly in the target as we move away from the stagnation point. The distributions of $I$ in the deforming penetrator and target regions are shown in Fig. 6. Also plotted in this figure is the variation of $I$ on the axial line. These plots reveal that significant deformations of the penetrator occur within the hemispherical region of radius nearly 2.0 and centered at the stagnation point. The values of $I$ near the stagnation point are quite high in the penetrator and target regions. As for the values of $p$, the value of $I$ on the axial line also drops quickly in the penetrator and slowly in the target as we move away from the stagnation point.

In order to see whether or not sharp gradients of $I$ occur across the target/penetrator interface $\Gamma_i$, we have plotted in Fig. 7 the variation of $I$ along three arbitrarily selected lines $LM$, $PQ$ and $PS$. The abscissa in these figures is the distance from $\Gamma_i$ of a point along the line

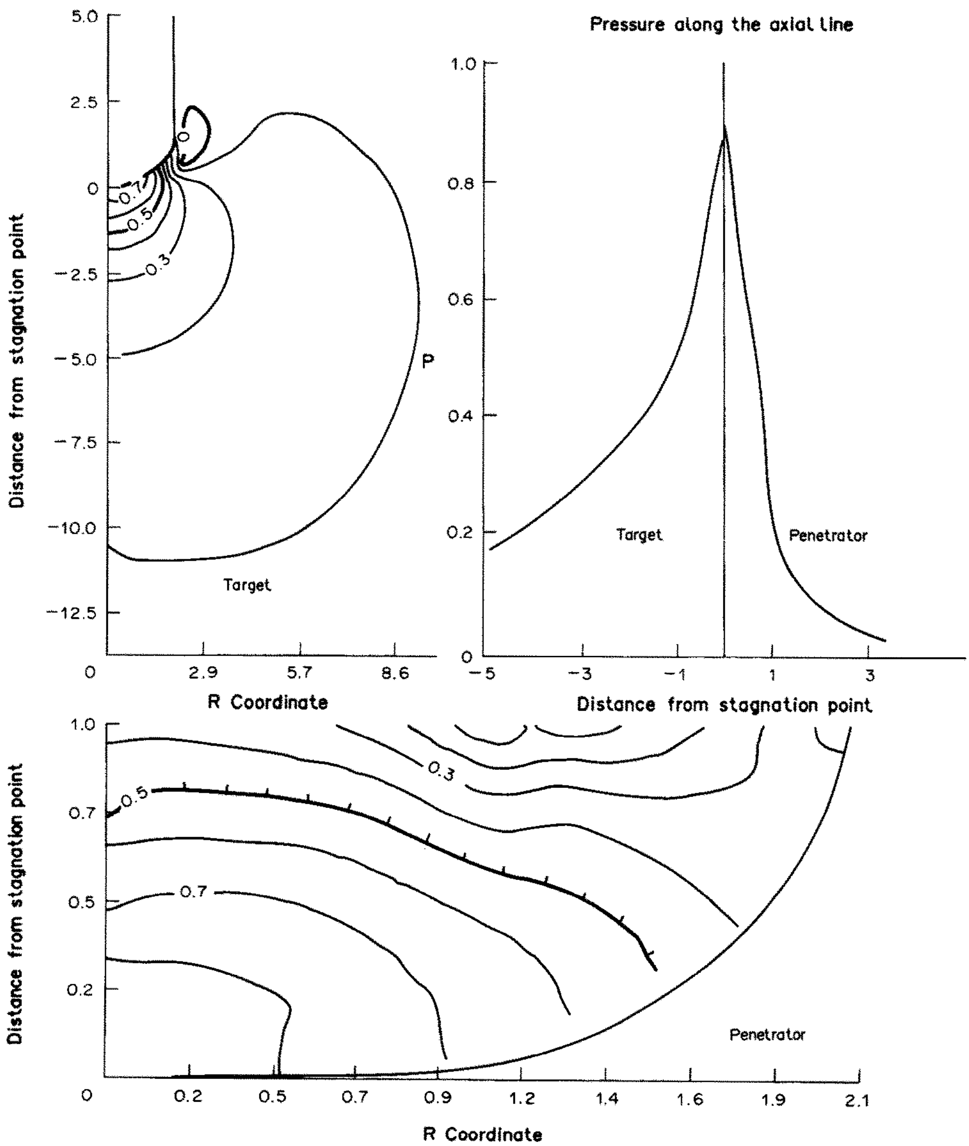


Fig. 5. Contours of non-dimensional hydrostatic pressure for $v_s = 600$ m/s.

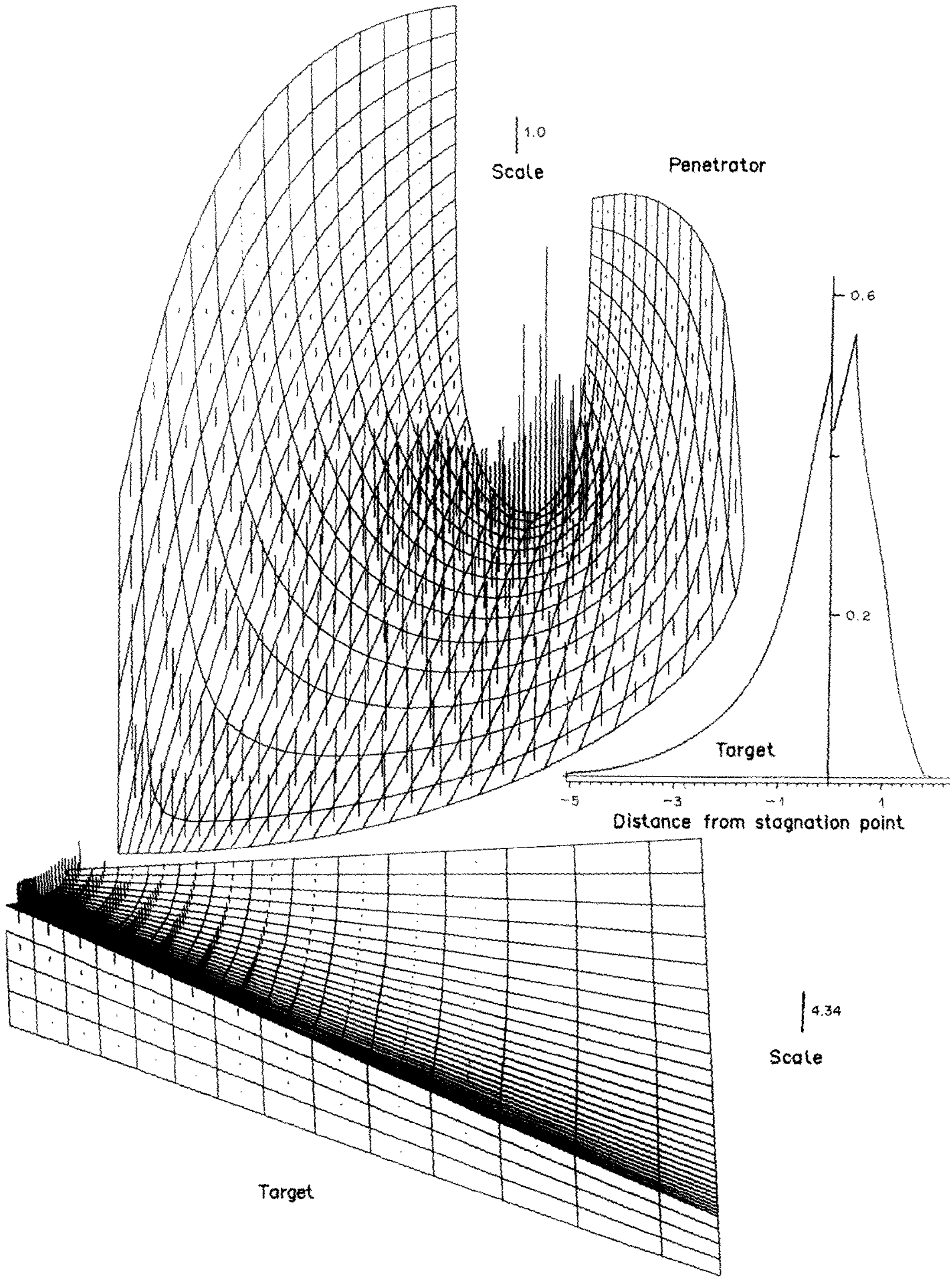


Fig. 6. Distribution of the second-invariant of the strain-rate tensor in the deforming penetrator and target regions and also on the axial line for $v_s = 600$ m/s.

considered. In each case $I$ is discontinuous across $\Gamma_i$. On line $LM$, $I$ for the target particle abutting $\Gamma_i$ is higher than that for the corresponding penetrator particle but the opposite holds for points on lines $PQ$ and $PS$. For points on $PQ$ and $PS$, sharp gradients of $I$ develop in the penetrator region whereas for points on $LM$, $I$ varies sharply for points on the target side. The value of $I$ at point $P$ where the penetrator particles undergo a change in the flow direction is considerably higher than that for the penetrator particles on line $PQ$ and $PS$. Since the

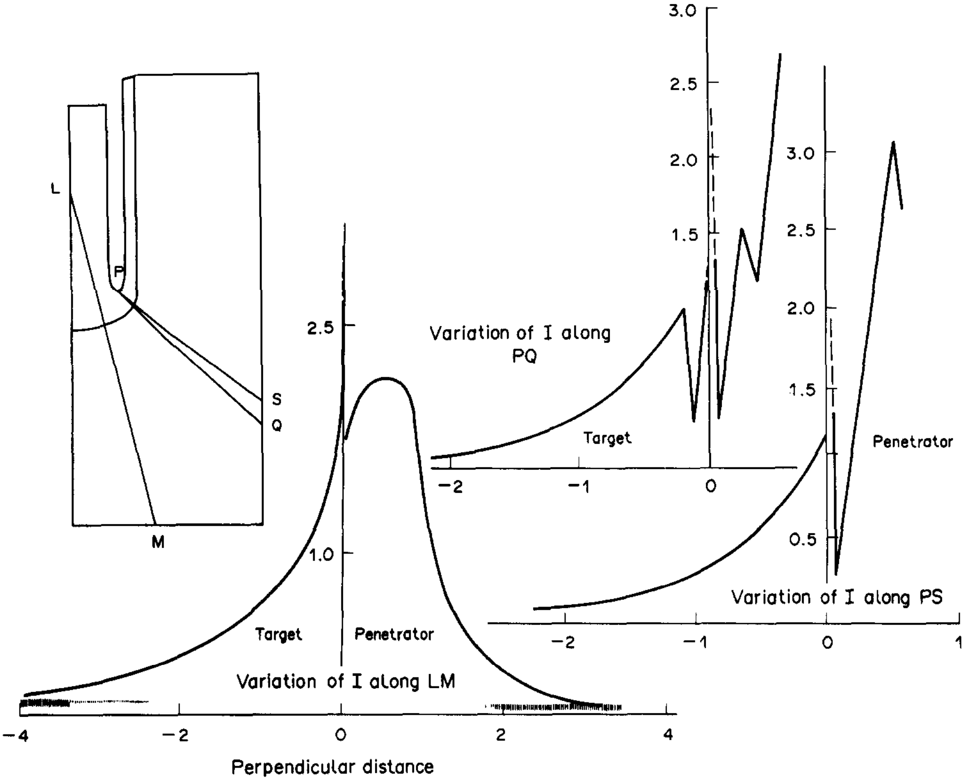


Fig. 7. Variation of the second invariant of the strain-rate tensor on three arbitrary selected lines for $v_s = 500$ m/s.

tangential velocity of target and penetrator particles abutting $\Gamma_i$ are nearly the same, for normal tractions to be continuous across $\Gamma_i$, normal derivatives of $\mathbf{v}$ on $\Gamma_i$ must be discontinuous if target and penetrator particles are made of different materials. This provides a justification for the jump in the value of $I$ as one crosses $\Gamma_i$. Recalling that the hydrostatic pressure contributes significantly to the normal tractions, it is not necessary that $I$ be sharply discontinuous across $\Gamma_i$ for the normal tractions on the two sides of $\Gamma_i$ to match with each other.

*Histories of field variables*

An outstanding problem in mechanics is the choice of the most appropriate constitutive model for the problem at hand. In general, the solution of a boundary-value problem depends strongly upon the constitutive model used. In order to determine which one of the many recently proposed theories [20–23] of large deformation elastoplasticity is suitable for a penetration problem, we compute histories of the hydrostatic pressure, second invariant of the strain-rate tensor and the spin for four penetrator and two target particles. These results should also help identify desirable testing regimes for practical problems.

The first step in finding the histories of a field variable is to plot the streamlines. Streamlines for four penetrator particles that once occupied the places $A(0.10, 5.88)$, $B(0.15, 5.88)$, $C(0.90, 5.88)$ and $D(0.95, 5.88)$, and two target particles sometime situated at $E(0.10, -3.12)$ and $F(0.15, -3.12)$ are shown in Fig. 8. That the streamlines do not intersect or merge together is clear from the blow up of the region enclosed in the box. In the discussion below we refer to the material particle that once occupied the place $A$ as the material particle $A$.

*Histories of field variables for penetrator particles.* Figure 9 shows, for $v_s = 500$ m/s, $(r, z)$ coordinates of the four penetrator particles at different non-dimensional times; the time being reckoned from the instant these particles occupied the aforestated places, and the non-dimensional time equals the physical time multiplied by $(v_s/r_0)$. The variation of the radial and axial components of the velocity of these particles is plotted in Fig. 10. Particles $A$ and $B$, initially near the axial line, arrive in the vicinity of the stagnation point at time $t \simeq 5$ when their

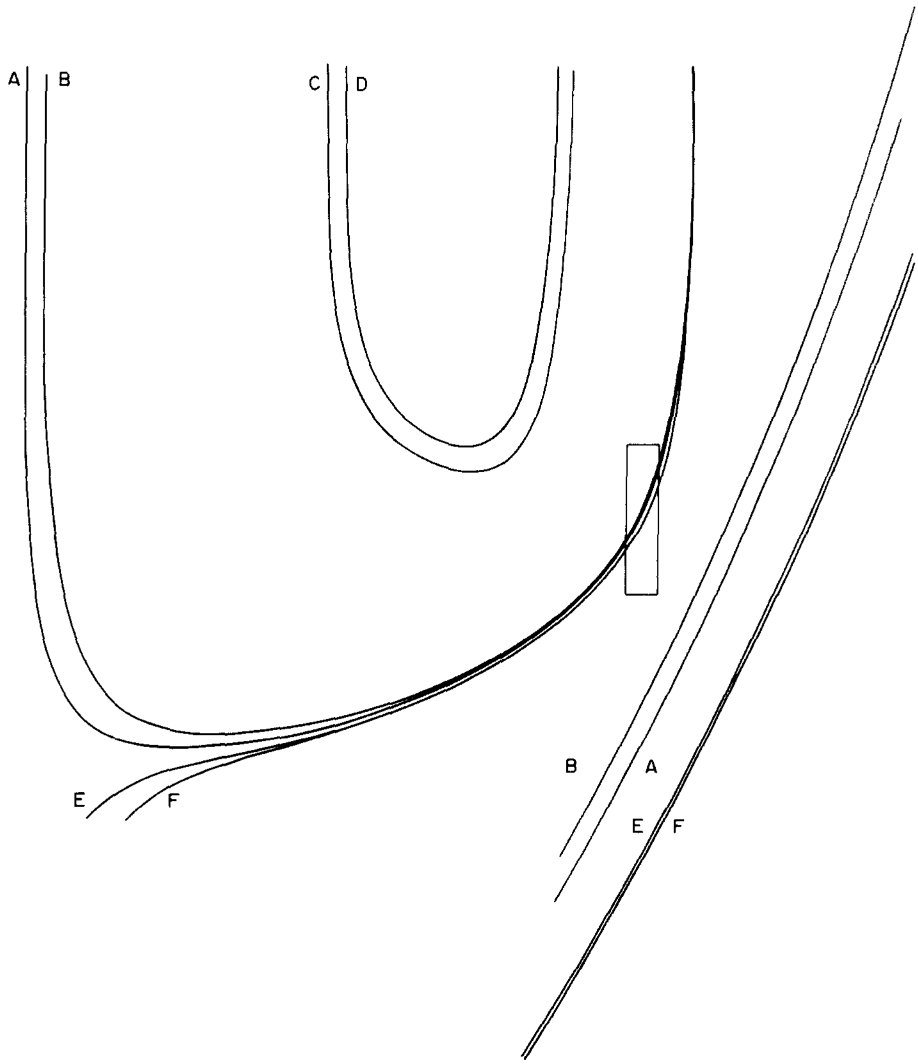


Fig. 8. Streamlines for four penetrator and two target particles for $v_s = 500$ m/s.

axial velocity relative to that of the stagnation point becomes zero. The radial velocity of these particles gradually increases, becomes maximum just before they begin turning upwards at $t \simeq 6.5$ and then decreases to zero quite rapidly. Material particles $C$ and $D$ that were initially close to the free surface of the penetrator approach near their bottom-most positions at $t \simeq 2.6$. Their radial velocity stays zero till they are close to their lowest positions, increases sharply and then decreases to zero equally rapidly too. In Fig. 11, we have plotted histories of the second invariant $I$ of the strain-rate tensor and of the plastic spin. Because the deformations are axisymmetric, there is only one non-zero component of total spin which equals the plastic spin since elastic deformations have been neglected. The peak values of $I$ and the plastic spin for material particles $C$ and $D$ are very large as compared to those for material particles $A$ and $B$. For particles $C$ and $D$, the magnitude of the plastic spin is either comparable or slightly larger than the value of $I$, and the peak values of $I$ and the plastic spin occur at almost the same instant. For these particles, $I$ and the plastic spin increase or decrease in tandem. Peak values of $I$ at particles $A$ and $B$ occur after their axial component of velocity has changed sign, i.e. they are moving upwards as observed from the stagnation point. Whereas $I$ for these particles increases quite rapidly and stays large for an extended period of time, the magnitude of the plastic spin for them increases slowly at first and once these particles are close to the stagnation point, the spin increases rapidly, and subsequently drops to zero at even a faster rate. The histories of the non-dimensional hydrostatic pressure shown in Fig. 12 reveal that for material

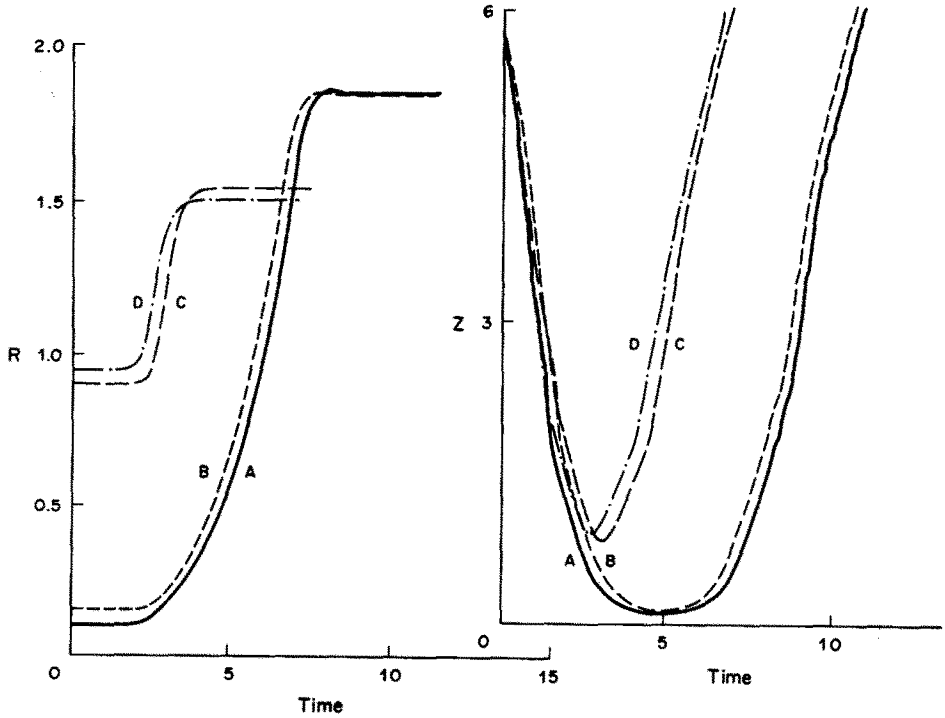


Fig. 9. $r$ and $z$-coordinates at different times of the four penetrator particles.

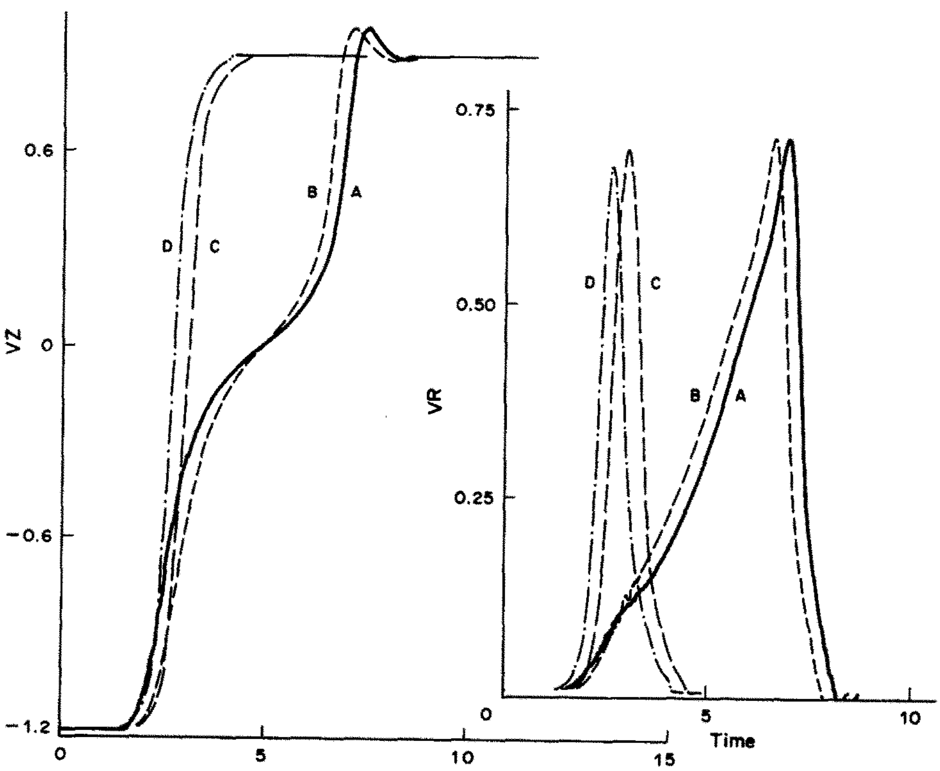


Fig. 10. The variation with time of the axial and radial velocity of the four penetrator particles.

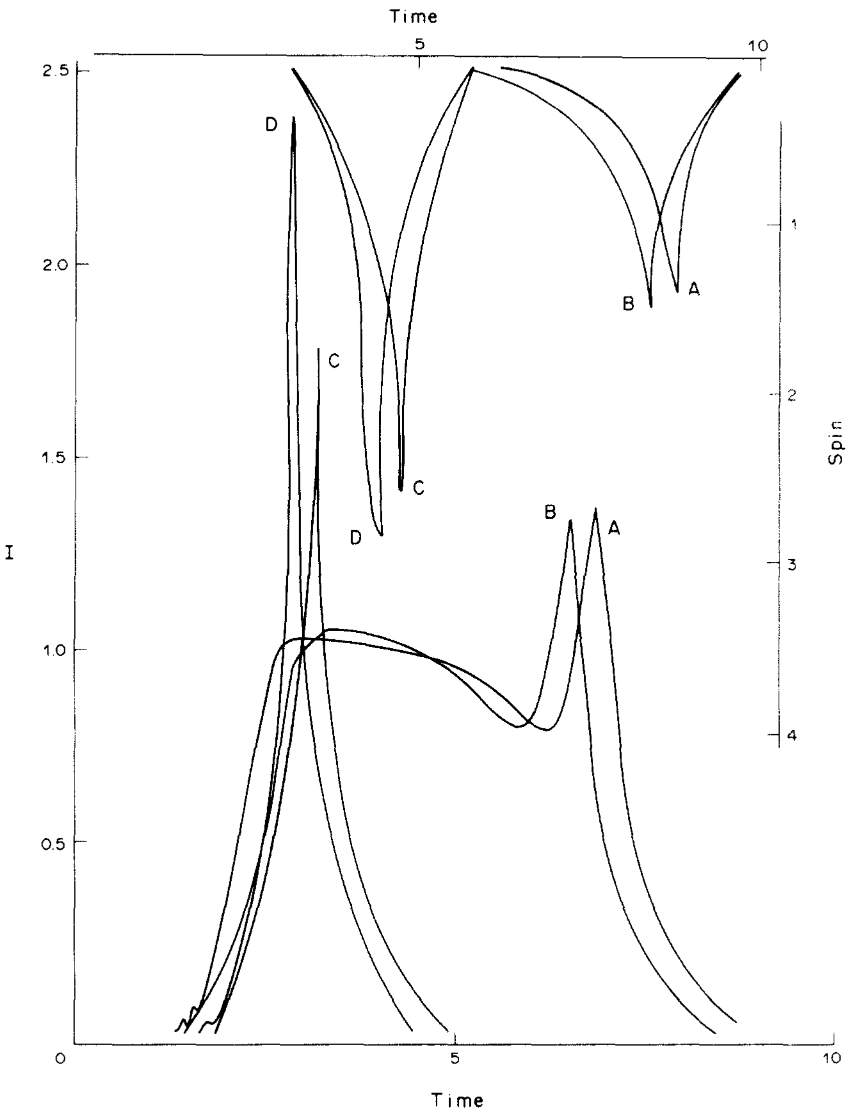


Fig. 11. Histories of the second invariant of the strain-rate tensor and the plastic spin for the four penetrator particles.

particles $A$ and $B$, $p_{max}$ is very large as compared to that for particles $C$ and $D$. This is because particles $C$ and $D$ are close to the traction free surface of the penetrator.

*Histories of field variables for target particles.* Figure 13 depicts the $r$- and $z$-coordinates and the radial and axial components of the velocity of the two target particles $E$ and $F$ at different times. As these particles approach the stagnation point $z = 0$ at $t \simeq 7$, their radial velocity begins to increase sharply, becomes maximum at $t = 7.5$ and 6.5, respectively, for $E$ and $F$, then rapidly decreases to zero. Their axial velocity relative to that of the stagnation point exhibits the reverse trend, i.e. it decreases to zero at $t \simeq 4.5$ and then increases gradually, the rates of decrease and increase of the axial velocity are nearly the same. The histories of the second invariant of the strain-rate tensor and the plastic spin for these two particles are exhibited in Fig. 14. Even though the values of $I$ for these particles gradually increase till $t \simeq 5$, their plastic spin stays zero. At about $t \simeq 5$, both the values of $I$ and of the plastic spin increase rapidly. The peak values of the plastic spin for these particles equal nearly twice the peak values of $I$ for them. The plastic spin decreases to zero much faster than $I$. The history of the non-dimensional hydrostatic pressure for these particles is shown in Fig. 12. Peak values, equal to $14.2\sigma_{0t}$, of the hydrostatic pressure at these particles occur when they are close to the stagnation point. Once

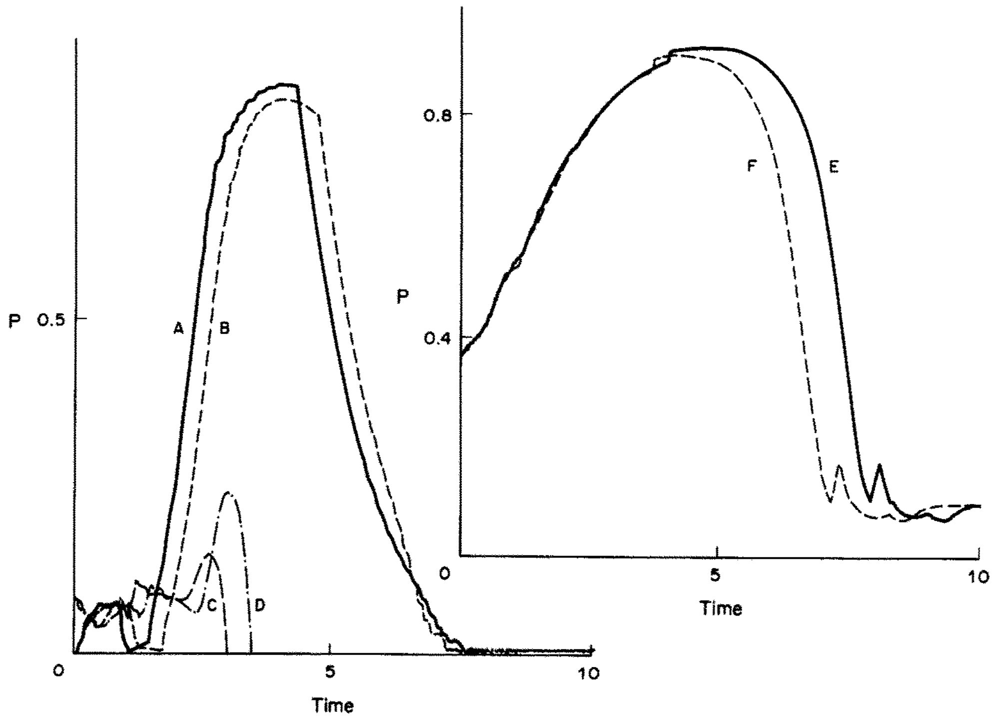


Fig. 12. Histories of the hydrostatic pressure for four penetrator and two target particles.

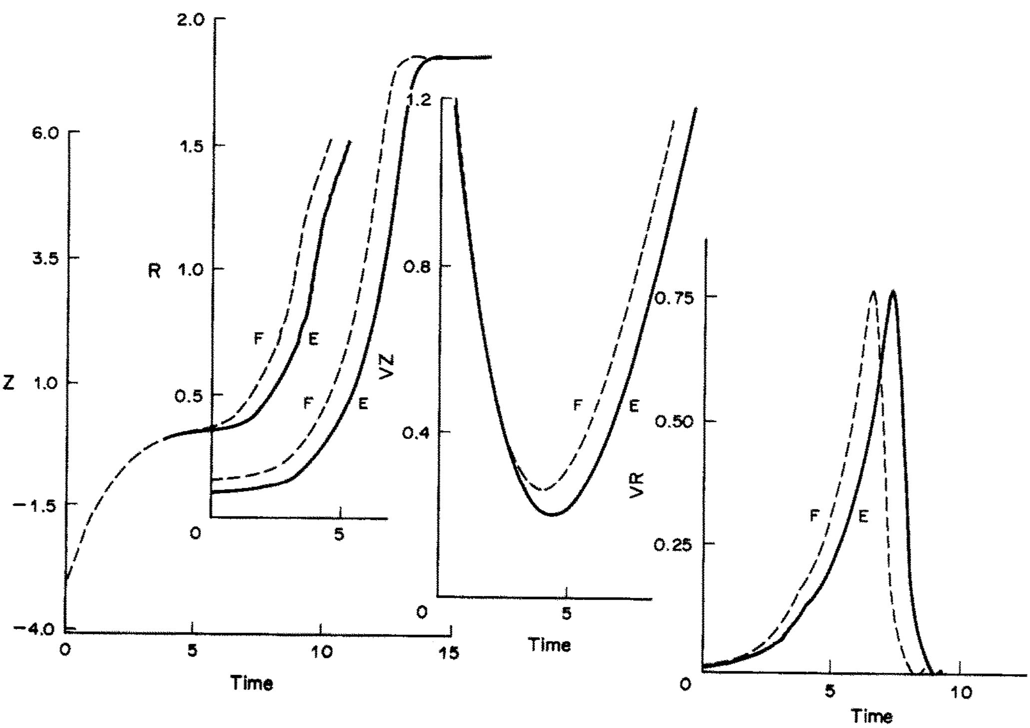


Fig. 13. The variation with time of $r$ and $z$-coordinates, and the axial and radial velocity of the two target particles.

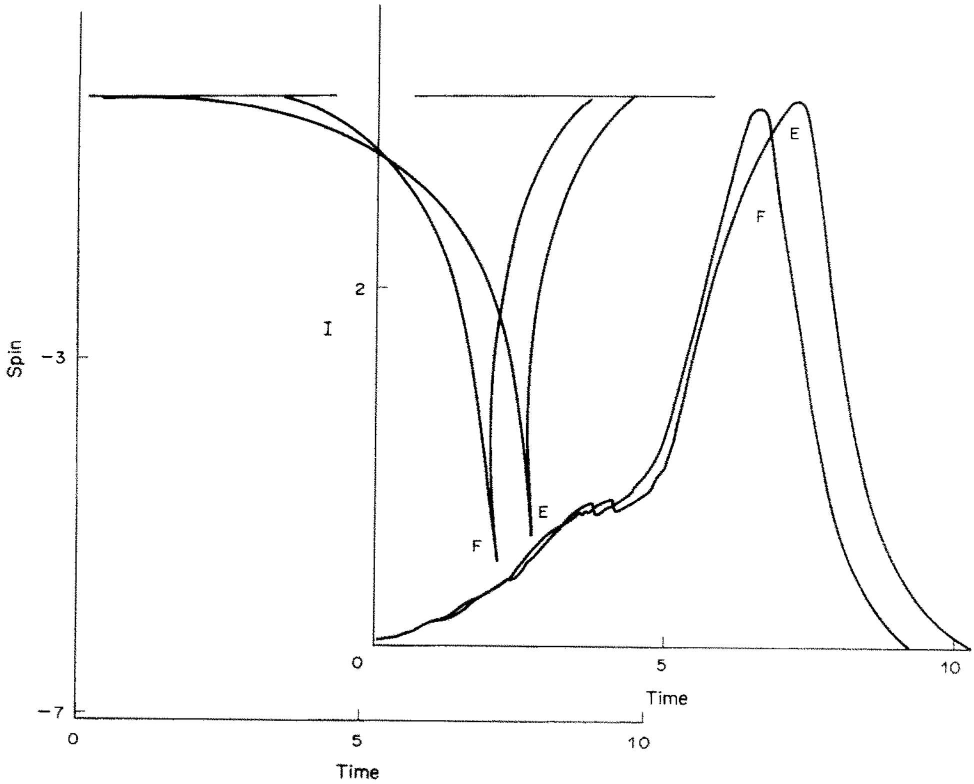


Fig. 14. Histories of the second invariant of the strain-rate tensor and the plastic spin for the two target particles.

these particles leave the area surrounding the stagnation point, the hydrostatic pressure decreases rather rapidly to zero.

## CONCLUSIONS

We have studied the penetration of a rigid/perfectly plastic rod penetrating into a thick rigid/perfectly plastic target when the deformations of both as seen by an observer situated at the stagnation point and moving with it are steady. It is found that the shape of the common interface near the stagnation point is ellipsoidal, and significant deformations of the penetrator occur in the hemispherical region of radius $2r_0$ centered at the stagnation point; $r_0$ being equal to the radius of the undeformed cylindrical portion of the rod. The axial resisting force experienced by the penetrator and the hydrostatic pressure near the stagnation point depend strongly upon the non-dimensional parameter $\alpha = \rho v_s^2/\sigma_0$ where $\rho$ is the mass density, $v_s$ the speed of the stagnation point and $\sigma_0$ is the yield stress of the material in a quasistatic simple compression test. For the three speeds considered, the crater radius was found to vary from $1.75r_0$ to $1.92r_0$. The values of the resistive strength parameters introduced by Tate [2] and Alekseevskii [3] depend upon the penetration speed $v_s$ and also on ratio $\rho_t/\rho_p$ of the mass densities. The peak values of the plastic spin experienced by a penetrator or a target particle either equal or exceed the peak values of the second invariant $I$ of the strain-rate tensor for it. Thus, plasticity theories which properly account for the evolution of the high plastic spin and deformation induced anisotropy ought to be employed in the study of penetration problems.

*Acknowledgements*—This work was supported by the U.S. Army Research Office Contract DAAL03-89-K-0050 to the University of Missouri–Rolla. Some of the computations were performed on the NSF sponsored supercomputer center at the University of Illinois–Urbana.

## REFERENCES

[1] A. TATE, *J. Mech. Phys. Solids* **15**, 387–399 (1967).
[2] A. TATE, *J. Mech. Phys. Solids* **17**, 141–150 (1969).
[3] V. P. ALEKSEEVSKII, *Comb. Expl. Shock Waves* **2**, 63–66 (1966). (Translation from Russian, Faraday Press, New York.)
[4] P. H. PIDSLEY, *J. Mech. Phys. Solids* **32**, 315–333 (1984).
[5] M. E. BACKMAN and W. GOLDSMITH, *Int. J. Engng Sci.* **16**, 1–99 (1978).
[6] M. RAVID and S. R. BODNER, *Int. J. Engng Sci.* **21**, 577–591 (1983).
[7] M. RAVID, S. R. BODNER and I. HOLCMAN, *Int. J. Engng Sci.* **25**, 473–482 (1987).
[8] M. J. FORRESTAL, K. OKAJIMA and V. K. LUK, *J. Appl. Mech.* **55**, 755–760.
[9] J. A. ZUKAS, T. NICHOLAS, H. F. SWIFT, L. B. GRESZCZUK and D. R. CURRAN, *Impact Dynamics*. Wiley-Interscience, New York, (1982).
[10] T. Z. BLAZYNSKI, in *Materials at High Strain Rates* (Edited by T. Z. BLAZYNSKI). Elsevier, New York (1987).
[11] E. W. BILLINGTON and A. TATE, *The Physics of Deformation and Flow*. McGraw-Hill, New York (1981).
[12] M. MACAULEY, *Introduction to Impact Engineering*. Chapman & Hall, London, (1987).
[13] R. C. BATRA and T. W. WRIGHT, *Int. J. Engng Sci.* **24**, 41–54 (1986).
[14] R. C. BATRA, *Int. J. Engng Sci.* **25**, 1131–1141 (1987).
[15] R. C. BATRA, *Comp. Mech.* **3**, 1–12 (1988).
[16] R. C. BATRA and PEI-RONG LIN, *Int. J. Engng Sci.* **26**, 183–192 (1988).
[17] R. C. BATRA and P. R. LIN, *Int. J. Impact Engng* **8**, 99–113 (1989).
[18] R. C. BATRA and P. R. LIN, *Int. J. Engng Sci.* **28**, 93–98 (1990).
[19] P. R. LIN and R. C. BATRA, *Int. J. Engng Sci.* **27**, 1155–1165 (1989).
[20] E. H. LEE, *J. Appl. Mech.* **36**, 1 (1969).
[21] L. ANAND, *J. Appl. Mech.* **47**, 439 (1980).
[22] S. NEMAT-NASSER, Micromechanically based finite plasticity. *Proc. Symp. Plasticity Today* (Edited by A. SAWCZUK). Elsevier, London (1983).
[23] Y. F. DAFALIAS, A simple illustration of the plastic spin concept and its role in finite plastic transformation. *Proc. Current Theories of Plasticity and their Applications*. University of Oklahoma–Norman (1984).
[24] A. TATE, *Int. J. Mech. Sci.* **28**, 599–612 (1986).
[25] R. C. BATRA and XINGJU CHEN, *Int. J. Engng Sci.* **28**, 1347–1358 (1990).
[26] T. GOBINATH and R. C. BATRA, Analysis of a steady state axisymmetric penetration problem. In *Computational Techniques for Contact, Impact, Penetration and Perforation of Solids* (Edited by L. E. SCHWER, N. J. SALAMON and W. K. LIU), ASME AMD, Vol. 103, pp. 235–247 (1989).
[27] A. N. BROOKS and T. J. R. HUGHES, *Comput. Meth. Appl. Mech. Engng* **32**, 199–259 (1982).
[28] A. TATE, *Int. J. Engng Sci.* **16**, 858 (1978).

*(Revision received and accepted 29 January 1991)*